



Research paper

Localized advanced ship predictor for maritime situation awareness with ship close encounter

Yufei Wang^{a,*}, Lokukaluge Prasad Perera^{a,b}, Bjørn-Morten Batalden^a

^a Department of Technology and Safety, UiT The Arctic University of Norway, Tromsø, Norway

^b SINTEF Digital, Oslo, Norway

ARTICLE INFO

Keywords:

Maritime situation awareness
Ship trajectory prediction
Kinematic motion models
Gated recurrent unit
Pivot point

ABSTRACT

The marine navigation environment can become further complex when ships with different autonomy levels are introduced. To ensure navigation safety in such a mixed environment, advanced ship predictor type technologies are essential in aiding ship navigators to attain the highest levels of situation awareness (SA). Consequently, precise ship trajectory prediction, specifically within a short prediction horizon, should be included in such predictors as an indispensable component. This study introduces two methods for ship trajectory prediction on a local scale: the kinematic-based method and the Gate Recurrent Unit (GRU)-Pivot Point (PP)-based method. The first method utilizes kinematic motion models to predict a ship trajectory. In the second method, the GRU is trained to generate the predictions of related ship navigation states. The ship's PP is then extracted from these predicted states, subsequently providing the predicted ship trajectory. Both methods are validated using simulated maneuvering exercises to assess their effectiveness, with a prediction horizon of 90 s. The results show that the kinematic-based method excels in the predictions during ship's stable stages, i.e., steady-state conditions. Meanwhile, the GRU-PP-based method exhibits robust performances in cases when new rudder orders are executed, i.e., transient conditions. It is considered that these applications can provide significant benefits in maritime SA in present and future ship navigation.

1. Introduction

1.1. Complex navigation environment

In recent years, significant progress has been made in the development of autonomous ships, propelled by advancements in sensor technologies, artificial intelligence, and the Internet of Things (UiT, 2021; Birkeland, 2022; MEGURI2040, 2022; AVATAR, 2023; Kongsberg, 2023). The ongoing research and development of autonomous ships aim to revolutionize the industry by tackling several critical challenges. These challenges include reducing maritime accidents attributable to human errors (Hoem et al., 2019; Kohn et al., 2019), improving energy efficiency to reduce greenhouse gas emissions (Munim, 2019; Kim et al., 2021), and alleviating shortages of skilled and professional seafarers (Porathe et al., 2014; Wróbel et al., 2017).

Until the present time, the definitions of ships' autonomy level can be found in various institutions and research studies (NFAS, 2017; IMO, 2019; Rødseth, 2019; Fukuto, 2021). As for the development of

autonomous ships, it is important to acknowledge that it is not realistic to implement the same autonomous levels to various ship types and flags simultaneously. Even with the same degree of autonomy, ships can manifest unique individual variations. Consequently, it is considered that close encounter situations among ships can become significantly complex when ships with varying levels of autonomy—such as fully autonomous, remotely-controlled, and manned ships—coexist within the same navigation area (Perera, 2019; Chang et al., 2021; Kim et al., 2022).

Considering this complexity, maneuvering and navigating to avoid potential collisions can pose significant challenges. One of the challenges lies in communication. Conventional manned ships primarily communicate directly through radio, visual, or audio signals. However, communication with remotely-operated or autonomous ships may adopt varied styles and utilize different protocols. Coordinating and ensuring seamless communication among ships with different autonomy levels can thus present challenges (Ait Allal et al., 2020; Koo et al., 2023). Some studies also suggest that due to the reliance of remotely-operated

* Corresponding author.

E-mail address: yufei.wang@uit.no (Y. Wang).

<https://doi.org/10.1016/j.oceaneng.2024.117704>

Received 19 January 2024; Received in revised form 18 March 2024; Accepted 27 March 2024

Available online 4 May 2024

0029-8018/© 2024 The Authors. Published by Elsevier Ltd. This is an open access article under the CC BY license (<http://creativecommons.org/licenses/by/4.0/>).

and autonomous ships on designed algorithms, it can be challenging for human operators to grasp how remotely-operated and autonomous ships perceive and respond to a complex and varying navigation environment (Abilio Ramos et al., 2019; Veitch and Andreas Alsos, 2022). Given that remotely-controlled and autonomous ships can rely heavily on various sensors to perceive their surroundings, it is crucial to examine the sensors' capabilities. This includes the understanding of how the limitations of sensors' performance could affect SA (Thombre et al., 2022). It is also worth noting that cybersecurity needs to be emphasized for remotely-operated and autonomous vessels since they can be susceptible to cyberattacks (Amro et al., 2022; Oruc et al., 2022). All the challenges mentioned above emphasize the fact that maintaining SA in a complex navigation environment can differ from conventional shipping practices. Therefore, the development of innovative technologies and tools is essential to support the future of maritime transportation.

1.2. Situation awareness in ship navigation

In maritime transportation, maintaining SA is vital to ensure the safety of ships, particularly in scenarios of close encounter situations. It is ruled therefore by the Convention on the International Regulations for Preventing Collisions at Sea (COLREGs) that all vessels shall at all times maintain a proper lookout by sight and hearing so that the operators can fully appraise the situations with the risk of collision. A common definition of SA is based on three ascending levels (Endsley, 1995): the perception of the elements in the environment within a volume of time and space; the comprehension of their meaning; and the projection of their status in the near future. Given the above-mentioned challenges in a complex navigation environment, it is considered that the importance of having the highest level of SA can be further emphasized (Perera and Batalden, 2019; Zhou et al., 2019; Rødseth et al., 2023). By assessing the current ship navigation states and predicting the evolution of the same states, navigators can proactively maneuver through challenging circumstances. This ability is particularly advantageous for maneuvering in congested areas, narrow passages, and high-traffic zones (Lee et al., 2016; Lu et al., 2018). Meanwhile, considering the longer response times of large-tonnage ships when making adjustments in rudder or engine power, proactive maneuvering is also required (Wickens et al., 2019). Furthermore, it is important to acknowledge that unforeseen events can occur at any time, especially among ships operating at different autonomy levels. Accurate predictions can aid navigators in creating temporal and spatial buffers, affording them the necessary margin and flexibility to effectively address these unexpected events.

The integration of sophisticated technologies like Global Navigation Satellite Systems (GNSS), advanced gyroscopes, Inertial Measurement Units (IMUs), Automatic Identification System (AIS), Electronic Chart Display and Information System (ECDIS), Advanced Precision Radar Aids (APRA), and other navigation systems significantly contributes to enhancing maritime SA. With the aid of these technologies and equipment, improving perception and understanding of nearby situations becomes achievable, particularly in scenarios with limited visibility. However, it is crucial to note that many of these systems still rely on simplistic linear mathematical models for ship trajectory prediction (Perera, 2017). Linear predictions may pose a risk of significant errors, particularly by overlooking potential collision points in close encounter situations. Therefore, the knowledge and experience of navigators continue to be a critical component in decision-making during close ship encounter situations.

1.3. Advanced ship predictors

The proposal of advanced ship predictors serves as innovative tools to enhance maritime SA and support decision-making processes. The workflow of advanced ship predictors can be segmented into different stages. Various methods and techniques are applied within these stages

to fulfill their respective functionalities. Considering the characteristics of ship maneuvering, it is proposed in (Perera and Murray, 2019) that advanced ship predictors should be utilized across both long time periods (global scale) and short time periods (local scale). The same study further suggest that global-scale prediction can be primarily based on AIS data, while local-scale prediction mainly utilizes measurements from onboard sensors such as GNSS systems, gyroscopes, IMUs, and others.

For the prediction on a local scale, it can be generally segmented into two stages: ship navigation state estimation and trajectory prediction. The KF-based techniques are widely employed in the first stage to estimate the required ship navigation states by fusing various onboard sensors' measurements (Bar-Shalom et al., 2002; Perera et al., 2012; Wang et al., 2023a,b). These estimates can subsequently be used to predict the ship trajectory in the second stage through various methods. One method is to directly employ the same models used in the KF-based techniques to predict trajectories. Particularly, the models can be combined with some practical tips in ship maneuvering so that the prediction can become more accurate and actionable. The implementation of a ship's pivot point is a good practice to support the local scale trajectory prediction (Perera, 2017). Another method involves employing different neural networks. Neural networks have proven effective in various domains, serving as powerful tools for addressing nonlinear problems. Furthermore, recent advancements in sensor and database technologies enable the collection and processing of large datasets, thus facilitating more efficient training of diverse neural networks. Many neural networks designed for ship trajectory prediction are trained using Automatic Identification System (AIS) datasets (Capobianco et al., 2020; Murray and Perera, 2021; Zhang et al., 2021). However, given the characteristics of AIS data, utilizing neural networks trained with AIS may not be the most suitable option for local scale predictions. These characteristics include data anomalies (Wolsing et al., 2022) and varying sampling rates (Artikis and Zissis, 2021). Several studies employ anomaly detection and linear interpolation techniques to preprocess the collected AIS data (Zhao et al., 2018; Suo et al., 2020). However, it is important to note that the predicted results have a relatively large time step and cover a wide navigation area. For local scale predictions that require more precise results with smaller time steps, these methods may not provide adequate support.

This study primarily focuses on the ship trajectory prediction on a local scale. Considering the importance of simulation verification before actual sea trials, the proposed method is currently being verified using simulated data from a ship bridge simulator. The remainder of the paper is structured as follows: Section 2 reviews the related research studies on advanced ship predictors; Section 3 offers detailed insights into the methods proposed and utilized in this study; Section 4 introduces the preparation for the simulation exercises and outlines the initialized parameters; Section 5 presents the simulation results and relevant discussions. Conclusions are drawn in the final sections of this paper.

2. Literature review

This review examines the methods and techniques utilized in the two stages of local scale predictions, namely ship navigation state estimation and trajectory prediction.

2.1. Ship navigation state estimation

In the first stage, the Kalman Filter (KF) and its variants—including the Extended Kalman Filter (EKF), Unscented Kalman Filter (UKF), Particle Filter (PF), and other related—are widely employed to estimate the ship navigation state. The implementation of KF-based state estimation requires system models that describe how the related system states evolve and how they are influenced by systematic uncertainties. Kinematic motion models are widely used in system modeling. External disturbances, such as external forces and moments, can be modeled as

uncertainties in these models. This treatment can reduce extensive efforts in identifying relevant hydrodynamic coefficients (Perera and Murray, 2019). Relevant studies on the implementation of kinematic motion models can be found in (Best and Norton, 1997; Perera and Guedes Soares, 2012; Wang et al., 2023a,b), where the applications of nonlinear system models like the Curvilinear Motion Model (CMM) and Constant Turn Rate and Acceleration (CTRA) are used to describe general ship behaviors. Regarding the kinematic motion models, it is important to note that the mathematical derivation processes of these models are rooted in a Cartesian coordinate, i.e., the Universal Transverse Mercator (UTM) coordinate system. A correction to address the project distortions in the UTM is suggested in the study by (Wang et al., 2023a,b), where the grid convergence is calculated to adjust ship headings in kinematic motion models.

In this study, the ship will be treated as a rigid body. This is based on the necessity to emphasize the relatively large geometric size of ships during short prediction periods. With the rigid body-based assumption, the ship's navigation states can exhibit variations at different locations (Batlle and Condomines, 2020). Therefore, when integrating kinematic motion models for a ship with the rigid body assumption, it is important to state the reference point at which the ship navigation state is characterized. Additionally, with the dispersion of onboard sensors across ships, it is also crucial to make adjustments to measurements associated with reference points.

2.2. Ship trajectory prediction

The prediction of a ship's trajectory typically starts from the current time step and relies on previously estimated navigation states. The kinematic motion models themselves can be directly employed to predict a ship's trajectory in the future, known as the kinematic-based method. In this method, it is assumed that the kinematic motion models remain applicable during the prediction horizon. However, it is essential to recognize that this assumption may not hold during a transient phase of ship maneuvering. For instance, the constant accelerations and yaw rates specified in the CMM and CTRA are not met when ships follow new rudder orders.

Predictions based on neural networks represent another popular prediction method. The remarkable capability of Recurrent Neural Networks (RNNs) in handling time-series data has gained notable attention in recent times. These kinds of networks are commonly preferred for making predictions due to their adaptation to utilizing internal states to process diverse input sequences (Lipton et al., 2015). However, RNNs with general structures face the challenge of vanishing or exploding gradients (Pascanu et al., 2013). In response to this issue, alternatives like RNNs with gated memory structures, such as Long Short-Term Memory (LSTM) (Hochreiter and Schmidhuber, 1997) and Gated Recurrent Unit (GRU) (Chung et al., 2014), are gaining more practical applications.

Ship trajectory prediction based on RNNs can be found in numerous research studies. In research (Murray and Perera, 2021), the authors employ the GRU with an encoder-decoder architecture to forecast ship trajectories. In another study (Capobianco et al., 2020), the authors combine the encoder-decoder architecture with the LSTM for ship trajectory prediction. Furthermore, several research studies propose modified structures of the RNNs, including bidirectional GRU (Wang et al., 2020), bidirectional LSTM (Zhang et al., 2021), and the combination of RNNs with Deep Neuron Network (DNN) (Li et al., 2022) and Convolutional Neural Network (CNN) (Syed and Ahmed, 2023). However, as previously mentioned, all these studies uniformly train the RNNs with AIS data. Therefore, it is considered that the corresponding predictions may lack precision at a local scale.

The GRU is chosen in this study and the datasets used for training are collected from the KF-based estimated navigation states. This is due to the limited quantity of these KF-based estimates compared to AIS. Many research studies state that the GRU outperforms LSTM with a relatively

smaller amounts of training data (Suo et al., 2020; Yang et al., 2020; Cahuantzi et al., 2023). Another feature of the used GRU is that the outputs are the surge and sway velocities, rather than positions and headings in a selected vessel. The surge and sway velocities obtained from the GRU are used to determine the location of the ship pivot point (PP).

2.3. Pivot point

The concept of a ship's PP has significant importance in ship maneuvering. Given that ships in general have substantial geometrical dimensions, turning maneuvers can result in expansive swept areas. Local-scale predictions must account for these areas. The size of the swept area is closely linked to the position of PP on ships (Seo, 2016). Therefore, the knowledge utilization of the PP serves as a fundamental technique in ship-handling education and training (Clark, 2005; Kjerstad, 2021). Experienced ship helmsmen usually rely on their expertise to estimate the PP, enabling them to predict ship positions and headings within a short time period.

The PP can be defined as follows: it is a specific point along the ship's centerline, measured from the ship's center of gravity (CG), where the sway velocity is zero during a turn maneuver (Tzeng, 1998). The distance between the ship CG and the PP— $dist_{CG \rightarrow PP}$ can be calculated as the ratio between the sway velocity at the CG (v_{CG}) and the yaw rate (r):

$$dist_{CG \rightarrow PP} = -v_{CG} / r \quad (1)$$

It should be noted that the determination of the PP based on (1) can pose challenges in real applications. One of the challenges arises from the effects of added mass in ship maneuvering. The added mass of a ship, also denoted as the extra mass of fluid that accelerates due to ship motions, can have the same comparable order of magnitude with respect to the ship mass (Fossen, 2011). This phenomenon highlights the importance of using the ship apparent center of gravity (ACG) rather than the CG when applying Newton's laws. However, the added mass can vary under different maneuvering and environmental conditions (Korotkin, 2008), making the ACG a non-fixed point. Another challenge lies in the calculation of the quotient in (1). It can become unstable when ships experience relatively small yaw rates. In such cases, the results may diverge and lack practical significance.

A novel approach to determine the position of PP is introduced in this study. In conventional ship maneuvering, it is well-known to experienced helmsmen that the PP of a turning ship typically situates around 1/5 to 1/4 of the ship length aft of the bow (Kjerstad, 2021). With this consideration, this study suggests that it can be more practical to estimate a range along the ship's centerline where the PP is likely to be found, rather than precisely determining the exact location of the PP.

3. Methodology

The complete workflow of the proposed localized advanced ship predictor development is depicted in Fig. 1. In Stage 1, the ship navigation states used in the kinematic motion models are estimated by the KF-based algorithm. The trajectory prediction in Stage 2 starts subsequently from the current step, utilizing the estimates obtained before. This paper primarily focuses on ship trajectory prediction; hence, the statistical properties and quality of the estimates from Stage 1 will not be addressed in this paper. For further details, reference can be made to (Wang et al., 2023a,b). This research study demonstrates that the estimated ship navigation states from the CMM and CTRA converge and maintain good precision. In this study, the ship trajectory prediction is carried out through two independent methods: the kinematic-based method and GRU-PP-based method. Both methods can generate a predicted trajectory that contains the ship's positions and headings over a shorter prediction horizon.

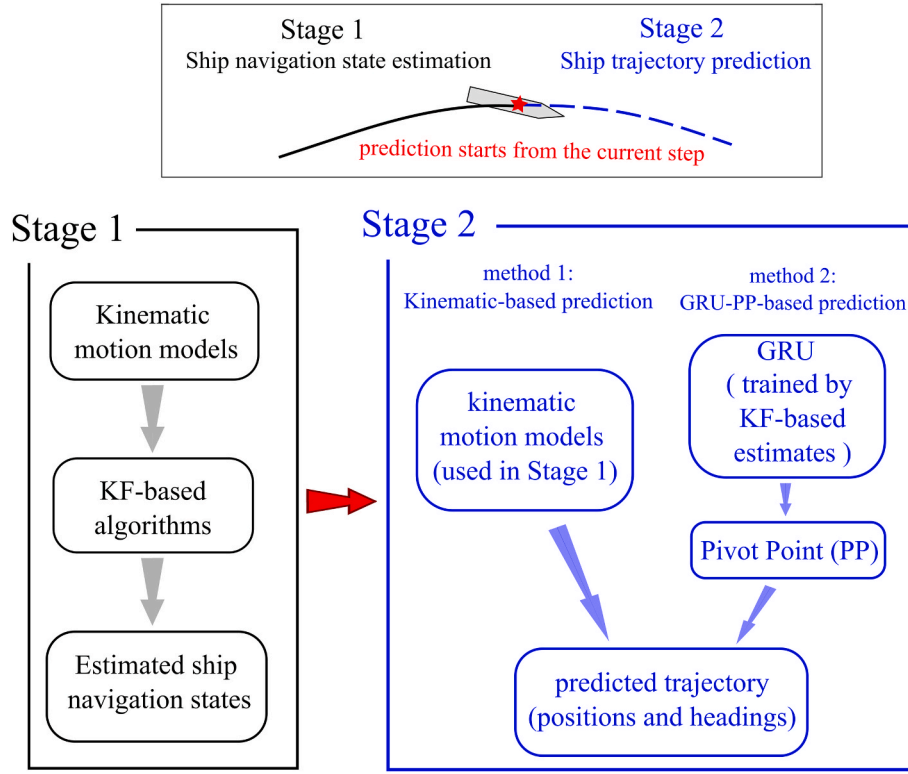


Fig. 1. The workflow of the localized advanced predictor involves two stages (Stage 2 is the primary focus of this paper).

3.1. Kinematic-based prediction

Three kinematic motion models are used in this section. The first model focuses on the rotation of the ship by using the constant angular acceleration (CAA) model (see Table 1). It can be observed that the CAA is a linear model (3), allowing the KF to generate optimal estimates. Additionally, this approach offers the advantage of deriving the angular acceleration \ddot{r} , which can be used for the correction of measurements. It should be noted that the heading ψ_T in the CAA is the true north. This configuration is based on the capability of advanced gyroscopes to directly measure ψ_T , as outlined in the measurement model of the CAA.

The other two models are the CTRA and CMM. Unlike the vessel states in the CAA, those in the CTRA and CMM must be explicitly defined with reference points on the ship. In the CTRA, two reference points P1 and P2 (see Table 2) are used. These two points are symmetrically positioned about the geometric center of the ship (C) and correspond to the measured positions by the GNSS system. The CTRA will consequently execute twice, providing vessel states in (6) with respect to both P1 and P2. Under the assumption that the ship's hull is incompressible, the velocity and acceleration (u and a_u) in the ship's surge direction is the same at both P1 and P2. The geometric center of the ship (C) is the

reference point in the CMM (see Table 3). It should be noted that the CAA will be executed prior to the CTRA and CMM. The estimated states of the CAA (2) can therefore be utilized as constant parameters in the CTRA and CMM.

With respect to the measured positions from the GNSS system, the raw data sets are latitude and longitude (z_φ, z_λ) in the geographic coordinate system. A conversion is thus necessary to transform these latitude and longitude coordinates into the corresponding northing and easting of the UTM coordinate system. In addition, it is important to emphasize that ψ_G in both the CMM and CTRA represents the grid north in relation to the northing. Another modification is thus required to convert the true north ψ_T into the grid north ψ_G . In this study, the functions $f_N(z_\varphi, z_\lambda)$ and $f_E(z_\varphi, z_\lambda)$ are used to calculate the related northing and easting from a collected (z_φ, z_λ). Furthermore, the function $f_\gamma(z_\varphi, z_\lambda)$ is used to calculate the grid convergence γ which is the difference between ψ_T and ψ_G . The details of the conversion functions of $f_N(\cdot)$, $f_E(\cdot)$ and $f_\gamma(\cdot)$ can be referred to (Kawase, 2013). As the onboard sensors are located in different positions, adjustments are also required for the measurement models (9), (10), and (14). These adjustments operate under the assumption that the ship's ACG is positioned around the geometric center of the ship, i.e., point C. The uncertainties related

Table 1
Constant angular acceleration (CAA) model.

	System model	Measurement model
<p>Gyroscope & IMU are in C z_{ψ_T} & z_r are provided</p>	$\mathbf{x}(t) = [\psi_T, r, \dot{r}]^T \quad (2)$ $\dot{\mathbf{x}}(t) = \begin{bmatrix} 0 & 1 & 0 \\ 0 & 0 & 1 \\ 0 & 0 & 0 \end{bmatrix} \bullet \mathbf{x}(t) + \mathbf{w}_x (\mathbf{w}_x \sim \mathcal{N}(\mathbf{0}, \mathbf{Q} \in \mathbb{R}^{3 \times 3})) \quad (3)$	$\mathbf{z}[t_k] = [z_{\psi_T}, z_r] \quad (4)$ $\mathbf{z}[t_k] = \begin{bmatrix} 1 & 0 & 0 \\ 0 & 1 & 0 \end{bmatrix} \mathbf{x}[t_k] + \mathbf{w}_z (\mathbf{w}_z \sim \mathcal{N}(\mathbf{0}, \mathbf{R} \in \mathbb{R}^{2 \times 2})) t_k = k \bullet \Delta t (k = 1, 2, \dots) \quad (5)$

Table 2
Constant turn rate & acceleration model (CTRA) (reference point: P1 & P2).

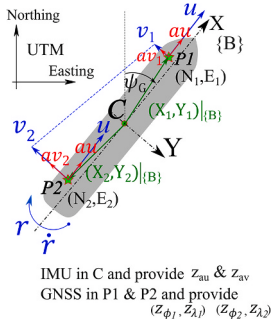
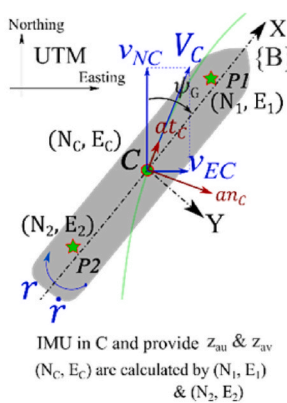
System model	Measurement model
 <p>IMU in C and provide z_{au} & z_{av} GNSS in P1 & P2 and provide $(z_{\phi_1}, z_{\lambda_1}), (z_{\phi_2}, z_{\lambda_2})$</p>	$x(t) = [N_i, E_i, u, v_i, au, av_i]^T \quad (6) \quad (i = 1, 2)$ $\dot{x}(t) = \begin{bmatrix} u \cos(\psi_G) - v_i \sin(\psi_G) \\ v_i \cos(\psi_G) + u \sin(\psi_G) \\ au \\ av_i \\ 0 \\ 0 \end{bmatrix} + w_x \quad (w_x \sim \mathcal{N}(\mathbf{0}, \mathbf{Q} \in \mathbb{R}^{6 \times 6})) \quad (7)$ <p>$i = 1, 2 \quad \psi_G = \psi_T - f_y(z_\phi, z_\lambda)$</p>
	$z[t_k] = [f_N(z_{\phi_1}, z_{\lambda_1}), f_E(z_{\phi_1}, z_{\lambda_1}), z_{au}, z_{av}] \quad (8)$ <p>For P1: $z[t_k] = \begin{bmatrix} N_1 \\ E_1 \\ au - v_1 r - \dot{r} Y_1 - r^2 X_1 \\ av_1 + u r + \dot{r} X_1 - r^2 Y_1 \end{bmatrix} + w_z \quad (9)$</p> <p>For P2: $z[t_k] = \begin{bmatrix} N_2 \\ E_2 \\ au - v_2 r - \dot{r} Y_2 - r^2 X_2 \\ av_2 + u r + \dot{r} X_2 - r^2 Y_2 \end{bmatrix} + w_z$ ($w_z \sim \mathcal{N}(\mathbf{0}, \mathbf{R} \in \mathbb{R}^{4 \times 4})$) (10)</p>

Table 3
Curvilinear motion model (CMM) (reference point: C).

system model	measurement model
 <p>IMU in C and provide z_{au} & z_{av} (N_C, E_C) are calculated by (N_1, E_1) & (N_2, E_2)</p>	$z[t_k] = [N_C, E_C, z_{au}, z_{av}] \quad (13)$ $z[t_k] = \begin{bmatrix} N_C \\ E_C \\ h_1 \cos(\psi_G) + h_2 \sin(\psi_G) - r g_1 \\ h_2 \cos(\psi_G) - h_1 \sin(\psi_G) + r g_2 \end{bmatrix} + w_z \quad (14)$ <p>($w_z \sim \mathcal{N}(\mathbf{0}, \mathbf{R} \in \mathbb{R}^{4 \times 4})$) (14)</p> <p>$N_C = 0.5(N_1 + N_2) + 3.6 \sin(\psi_G);$ $E_C = 0.5(E_1 + E_2) + 3.6 \cos(\psi_G);$ $\psi_G = \psi_T - f_y(z_\phi, z_\lambda);$ $h_1 = at_C f^{v_{NC}} - an_C f^{v_{EC}} + r v_{EC};$ $h_2 = at_C f^{v_{EC}} + an_C f^{v_{NC}} - r v_{NC};$ $g_1 = v_{NC} \cos(\psi) + v_{EC} \sin(\psi);$ $g_2 = -v_{NC} \sin(\psi) + v_{EC} \cos(\psi);$</p>
$x(t) = [N_C, E_C, v_{NC}, v_{EC}, at_C, an_C]^T \quad (11)$ $\dot{x}(t) = \begin{bmatrix} v_{NC} \\ v_{EC} \\ at_C f^{v_{NC}} - an_C f^{v_{EC}} \\ at_C f^{v_{EC}} + an_C f^{v_{NC}} \\ 0 \\ 0 \end{bmatrix} + w_x \quad (w_x \sim \mathcal{N}(\mathbf{0}, \mathbf{Q} \in \mathbb{R}^{6 \times 6})) \quad (12)$ $f^{v_{NC}} = \frac{v_{NC}}{\sqrt{v_{NC}^2 + v_{EC}^2}}$ $f^{v_{EC}} = \frac{v_{EC}}{\sqrt{v_{NC}^2 + v_{EC}^2}}$	

to this assumption are incorporated into the system and measurement noises.

The kinematic-based prediction utilizes the system models (3), (7), and (11). When the prediction starts, the estimated states (2), (6), and (11) from the current step are inputted into the system models to calculate the states for the next steps. This calculation can be iteratively executed until the defined prediction horizon is reached. The calculated positions and headings can thus be extracted to generate the ship's predicted trajectory. In this study, kinematic-based predictions are based on these two combinations of models: CAA + CMM and CAA + CTRA. The predicted headings are derived from the CAA, while the predicted positions are obtained from the CMM or CTRA. The measurement models (5, 9, 10, 14) will not be utilized in the trajectory prediction. Instead, they are employed in Stage 1 by the KF-based algorithms to produce estimated navigation states and the details can be seen in (Wang et al., 2023a,b).

3.2. GRU-PP-based method

The second prediction method integrates the GRU and the ship PP. The GRU is employed to generate the ship surge and sway velocities over the prediction horizon. These predicted states can later determine the location of the PP along the ship's centerline. After identifying the

location of the PP, the ship's movement can be decomposed into two components: the translation of an arbitrary point and the rotation around the PP. The ship's positions and headings can then be determined using a rigid body motion-based algorithm.

3.2.1. The gated recurrent unit

The GRU is a simplified version of the LSTM that aims to enhance computational efficiency. In contrast to the LSTM's three-gate structure,

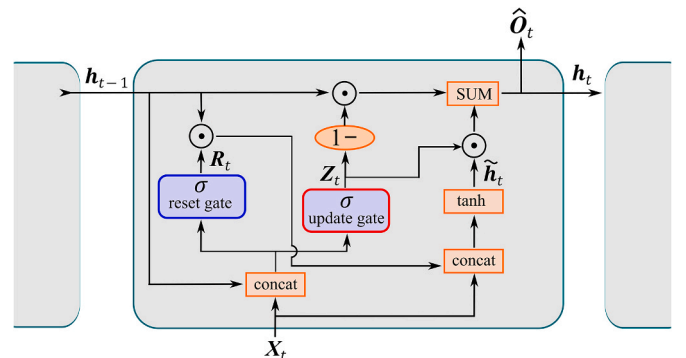


Fig. 2. GRU cell structure.

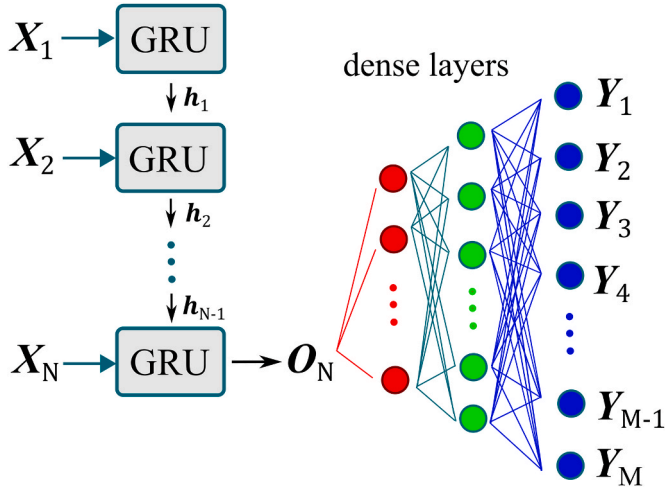


Fig. 3. The generation of predictions from the GRU and the attached dense layers.

the GRU simplifies the architecture to feature only two gates: the reset gate and the update gate. The two gates in the GRU can adaptively adjust the balance between the “remembering” and “forgetting” during the training process. Despite the reduction in the number of gates, the GRU incorporates a specialized mechanism aimed at achieving equivalent levels of accuracy to the LSTM. The cell of the GRU is shown in Fig. 2.

The reset gate and update gate work together to perform the regression of latent state h_t at each time step t . This procedure can be formulated in (15)–(18).

$$Z_t = \sigma(W_z X_t + U_z h_{t-1} + b_z) \quad (15)$$

$$R_t = \sigma(W_r X_t + U_r h_{t-1} + b_r) \quad (16)$$

$$\tilde{h}_t = \tanh(W_h X_t + U_h (R_t \odot h_{t-1}) + b_h) \quad (17)$$

$$h_t = (1 - Z_t) \odot h_{t-1} + Z_t \odot \tilde{h}_t \quad (18)$$

where X_t is the input vector, Z_t is the update gate vector, R_t is the reset gate vector, h_t is the latent state vector, \tilde{h}_t is the candidate activation vector, and O_t is the output vector. W , U , and b , each denoted with different subscripts, are related parameter matrices and vectors. The operators $\sigma(\cdot)$ and \odot represent the logistic activation function and Hadamard product, respectively. The update gate plays a pivotal role in adjusting the rate of new memories and determines the weights assigned to updating the long-term memory (15). The reset gate is responsible for regulating the rate of memory decay and generates the weights allocated

to resetting during memory processing (16). Following this, the reset value, denoted as R_t , is utilized to prepare \tilde{h}_t for the subsequent memory update (17). Finally, the long-term memory undergoes an update for h_t by utilizing a weighted ratio of h_{t-1} and \tilde{h}_t (18).

The output O_t from the final GRU cell is used to produce a time series of predictions via dense layers (see Fig. 3). In this study, the predictions ranging from Y_1 to Y_M represent the time series of the predicted surge and sway velocities, i.e., u , v_1 , and v_2 over the prediction horizon M . The input vector X_t is derived from the states outlined in (2), (6), and (11). During the training process, the Mean Square Error (MSE) is used as the loss function. The adjustment of parameters in the neural network are guided by the backpropagation algorithm, which is designed to minimize the MSE.

3.2.2. Training of the GRU

Since the training of the GRU must be conducted in advance, a series of historical simulated exercises of ship maneuvers is collected. One of the examples is depicted in Fig. 4. Following the workflow of Stage 1 (see Fig. 1), the ship’s navigation states depicted in (2), (6), and (11) can be acquired for the entire duration of maneuvering. Some states from (2), (6), and (11) are selected and processed to generate the vector denoted by X (19). The parameters δ and β_C in X are not the states in the kinematic models. δ represents the rudder order. β_C denotes the drift angle which is defined as the difference between the heading and the course. The course can be determined using the v_{NC} and v_{EC} as outlined in (11).

$$X = (\delta, \psi_G, r, \beta_C, V_C, at_c, an_c, au, av_1, av_2, u, v_1, v_2) \quad (19)$$

A time series of the vector (19) can be obtained which cover from t_0 to t_{end} . Since the GRU is introduced to improve prediction precision in scenarios where the selected ship executes new rudder orders, the training dataset only includes the vectors from a defined timeframe both before and after the release of the new rudder order. Fig. 5 illustrates the processing of training samples extracted from the time series of vector (19) shown in Fig. 4. Each training sample encompasses a time span of 30 s preceding the issuance of a new rudder order and 90 s following its execution. This configuration is based on the consideration that the well-trained GRU can effectively analyze historical navigation states occurring 30 s before a new rudder order to forecast subsequent states for the following 90 s. Given that the state estimation occurs at 0.1-s intervals, the input has a lag of 300 and the output spans a prediction horizon of 900 steps. The first ten elements in the vector (19) form the input of GRU. With the identical input, the GRU is structured to produce three distinct outputs: u , v_1 , and v_2 . Because these outputs are generated independently, the GRU thus requires three separate training processes for each distinct result.

A normalization procedure is also included to optimize the training

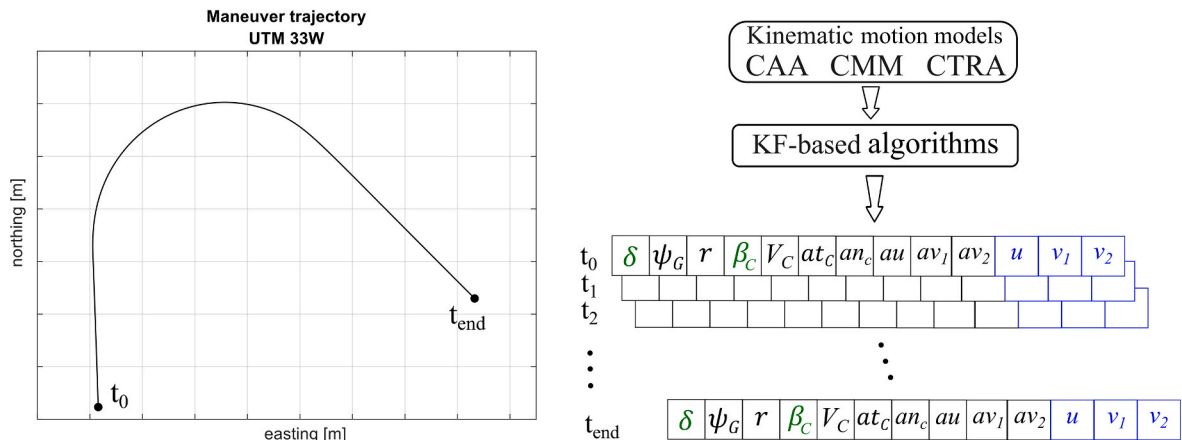


Fig. 4. Time series of the vector are generated from the estimated ship navigation states from a simulated exercise of maneuver.

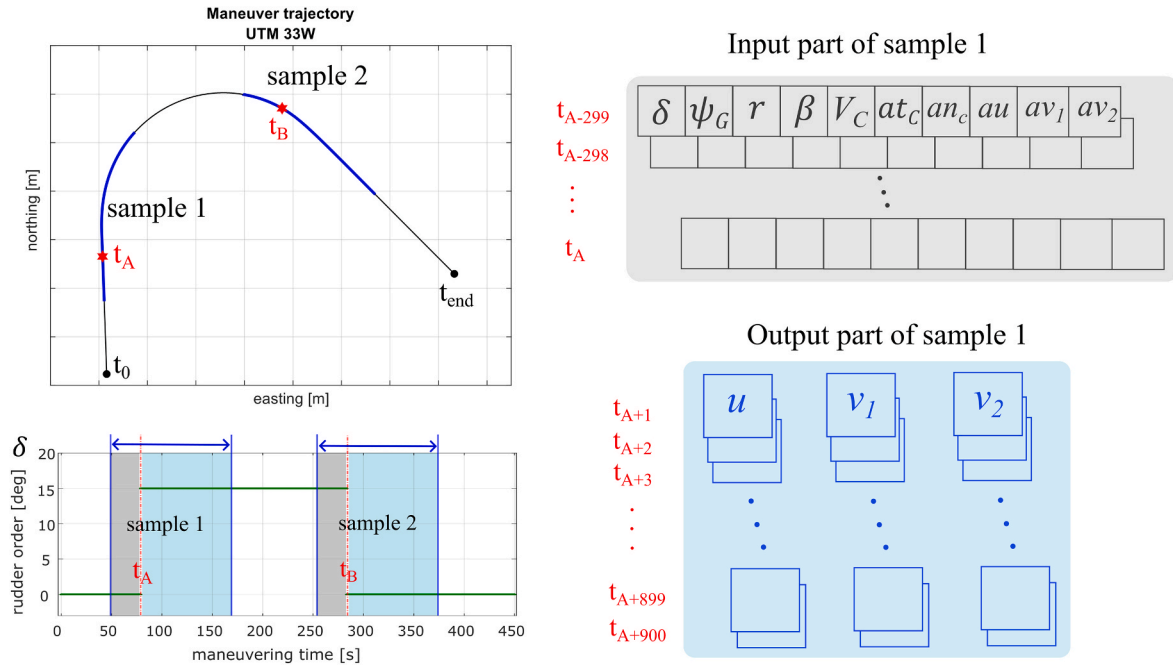


Fig. 5. Extracting training samples from a simulated exercise of maneuver. Each training sample spans a 120-s period, with new rudder commands issued at the 30th second of each interval (estimates are obtained in every 0.1[s]).

process. This procedure scales all the ship navigation states to fit within the -1 to 1 range, using the minimum and maximum values from the samples. Subsequently, a corresponding denormalization process will be applied to the outputs based on (20).

$$X_{train} = \frac{X - \min(X)}{\max(X) - \min(X)} \times 2 - 1 \quad (20)$$

($\max(\delta) = 45^\circ$, $\min(\delta) = -45^\circ$)

3.2.3. Rigid body-based algorithm

Since the ship is treated as a rigid body, its motions can be decomposed into translational and rotational motions. The motion decomposition of a rigid body may not be unique in some situations. However, for practical purposes in analyzing ship maneuvers, it is more beneficial to decompose the motion such that the translational movement aligns with

u and the rotational motion centers around the PP. It is crucial to differentiate the PP from the instant center of rotation. The depiction in Fig. 6 illustrates that the PP acts as the center for rotational movement concerning the ship's sway velocities, while also being involved in transitional motion. The assumption of a rigid body implies also that sway velocities are linearly distributed along the ship's length. With this premise, the position of the PP on the ship's centerline can be

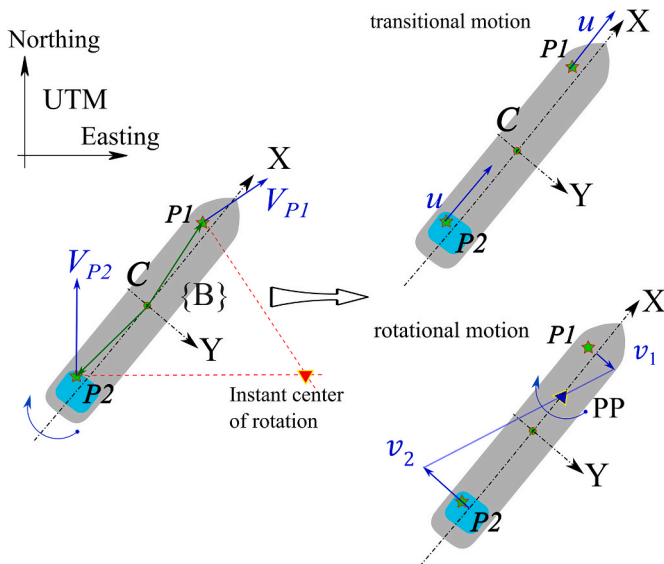


Fig. 6. Decomposition of the motion of a ship.

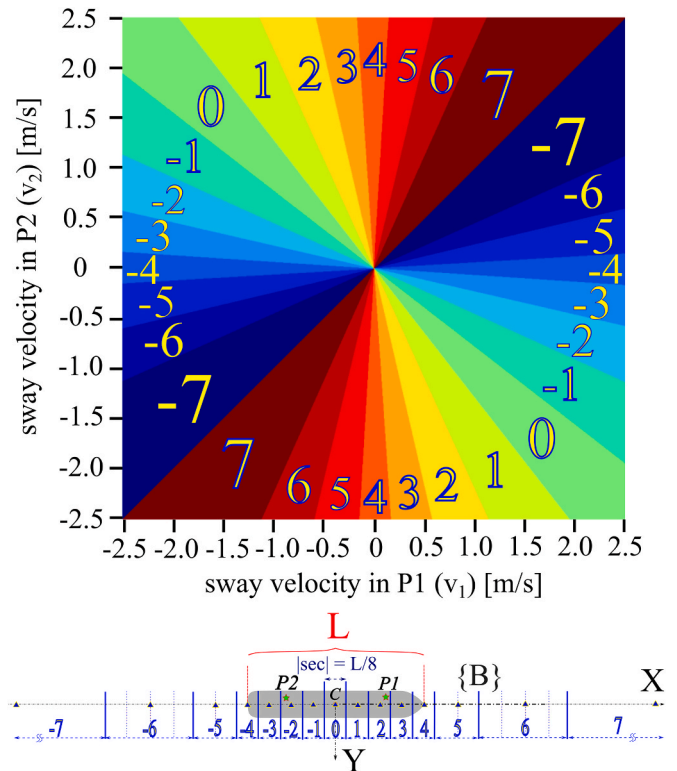


Fig. 7. The mapping between v_1 , v_2 , and predefined regions of pivot point.

Table 4
Predefined regions and pivot point position.

Region	Range in X-axis ($ sec = L/8$)	PP coordinate in X-axis of {B}
-7	$(-\infty, -10.5 \bullet sec)$	$-20 \bullet sec $
-6	$(-10.5 \bullet sec , -6.5 \bullet sec)$	$-8.5 \bullet sec $
-5	$(-6.5 \bullet sec , -4.5 \bullet sec)$	$-5.5 \bullet sec $
-4	$(-4.5 \bullet sec , -3.5 \bullet sec)$	$-4 \bullet sec $
-3	$(-3.5 \bullet sec , -2.5 \bullet sec)$	$-3 \bullet sec $
-2	$(-2.5 \bullet sec , -1.5 \bullet sec)$	$-2 \bullet sec $
-1	$(-1.5 \bullet sec , -0.5 \bullet sec)$	$-1 \bullet sec $
0	$(-0.5 \bullet sec , 0.5 \bullet sec)$	0
1	$(0.5 \bullet sec , 1.5 \bullet sec)$	$1 \bullet sec $
2	$(1.5 \bullet sec , 2.5 \bullet sec)$	$2 \bullet sec $
3	$(2.5 \bullet sec , 3.5 \bullet sec)$	$3 \bullet sec $
4	$(3.5 \bullet sec , 4.5 \bullet sec)$	$4 \bullet sec $
5	$(4.5 \bullet sec , 6.5 \bullet sec)$	$5.5 \bullet sec $
6	$(6.5 \bullet sec , 10.5 \bullet sec)$	$8.5 \bullet sec $
7	$(10.5 \bullet sec , \infty)$	$20 \bullet sec $

determined using v_1 and v_2 .

In this study, a mapping system is established to assign the PP to the predefined regions along the ship's centerline based on v_1 and v_2 . As shown in Fig. 7, these predefined regions are designated within the range of -7 to 7 , with a deliberate emphasis on concentration between the bow and stern (region -4 to 4). Moving away from both the bow and stern, the size of these regions is progressively expanded. This design is based on the experience with the selected vessel in the simulated maneuvering, where the PP is primarily located within the ship. Additionally, a rigid body motion-based algorithm is utilized to generate the predicted trajectory. When the PP is far from the ship, its precise numerical value gradually becomes of minimal impact on the algorithm's outcome. Therefore, the regions outside the ship are designed to expand progressively.

When allocating the PP to a specific region, a fixed distance between the PP and the ship's center (C) will be determined according to Table 4. The distance between the PP and C will be further converted into the distance between the PP and P2— $dist_{pp \rightarrow p2}$. As it is later demonstrated that the bridge and the GNSS are positioned around P2, the distance $dist_{pp \rightarrow p2}$ gains more practical significance.

Supported by this mapping system, the prediction of the ship's trajectory becomes feasible once the predicted u , v_1 , and v_2 are established from the GRU. The translational motion (L_{trans}) can be derived solely from u . Because the cargo carrier has the bridge located astern, the distance between PP and P2 ($dist_{pp \rightarrow p2}$) and v_2 are used to calculate the angular speed of the rotational motion (ω). It is evident that ω displays minimal sensitivity to the variation of $dist_{pp \rightarrow p2}$ when this distance is significantly large. This characteristic underlies the reason for the predefined regions that have relatively extensive ranges away from both the bow and stern of the vessel.

Given the ship navigation states in current time step t_k , and the time series of predictions of (u , v_1 , v_2) from time step t_{k+1} to t_{k+N} by the GRU, the predicted ship trajectory from t_{k+1} to t_{k+N} can be calculated by the

provided algorithm:

Rigid body motion-based algorithm for ship trajectory prediction:

Given ship navigation states in t_k , and prediction of u , v_1 , and v_2 from t_{k+1} to t_{k+N} for $i = k + 1$ to $k + N$ do:
(translational calculation)
 $L_{trans}[t_i] = u[t_i] \bullet dt$,
(rotational calculation)
determine the position of PP by $v_1[t_i]$ & $v_2[t_i]$ via the mapping system
calculate $dist_{pp \rightarrow p2}[t_i]$,
 $\omega[t_i] = \frac{v_2[t_i]}{dist_{pp \rightarrow p2}[t_i]}$,
(heading in next time step)
 $\psi_C[t_i] = \psi_C[t_{i-1}] + \omega[t_i] \bullet dt$,
(position of C in next time step)
 $N_C[t_i] = N_C[t_{i-1}] + L_{trans}[t_i] \bullet \cos(\psi_C[t_i])$,
 $E_C[t_i] = E_C[t_{i-1}] + L_{trans}[t_i] \bullet \sin(\psi_C[t_i])$.

It is worth noting that the operations of translational and rotational calculations in this algorithm are non-commutative. Different calculation sequences lead to discrepancies in prediction outcomes. To reduce these discrepancies, using a smaller value of dt is advisable.

4. Preparation for the simulation experiment

4.1. Simulation environment

All the maneuvering data sets used in this study are obtained from the simulated exercises conducted within the UiT bridge simulator (see Fig. 8). The bridge simulator serves as a platform for nautical education, enabling students to practice various maneuvers and enhance their seamanship skills. A substantial volume of ship exercise maneuvering data sets is thus accessible through the simulator. It is also important to highlight that maneuvers in the simulator are generated using specific nonlinear dynamic motion models that are unknown to the users. This reflects real-world navigation scenarios, where accurately capturing the dynamic properties of ships remains a challenging task.

A general cargo carrier (see Fig. 9) is selected from the simulator to generate various maneuvers. One should note that due to the relatively large size and tonnage of this cargo carrier, The primary method used to change ship navigation states, such as for collision avoidance, is the adjustment of the rudder rather than altering the engine power. Calm weather conditions are set during maneuvers so that the ship will not have significant pitch and roll motions. The cargo carrier is equipped with multiple sensors, including the gyroscope and IMU situated at a selected location of the ship that is closer to the vessel center of mass. Two GNSS antennas are symmetrically positioned relative to point C, recording the positional data of the bow (P1) and stern (P2), respectively. The measurements from these sensors will be used in the KF-based estimation to generate the required ship navigation states.

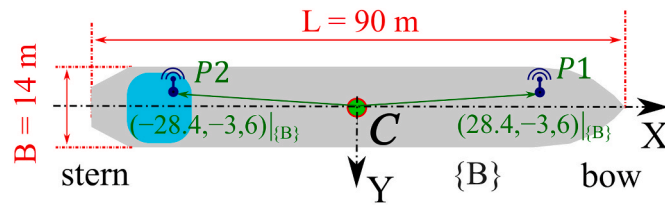


(a) View of the simulator from outside



(b) Inside the UiT bridge simulator

Fig. 8. The UiT bridge simulator.



The advanced gyroscope and IMU are installed in C;
The GNSS antennas are installed in P1 and P2.

Type of vessel	General Cargo Carrier
Dimensions	LOA 90.00 m/ Beam 14.00 m
Draft	Ca. 6.5 m
Max Speed	Ca. 11.5 knots
Main Engine / Propulsion:	MAK 6M 25 1,800 kW/ controllable pitch propeller
gross tonnage / net tonnage	2,999 t / 1,639 t

Fig. 9. The general cargo carrier used in the UiT bridge simulator.

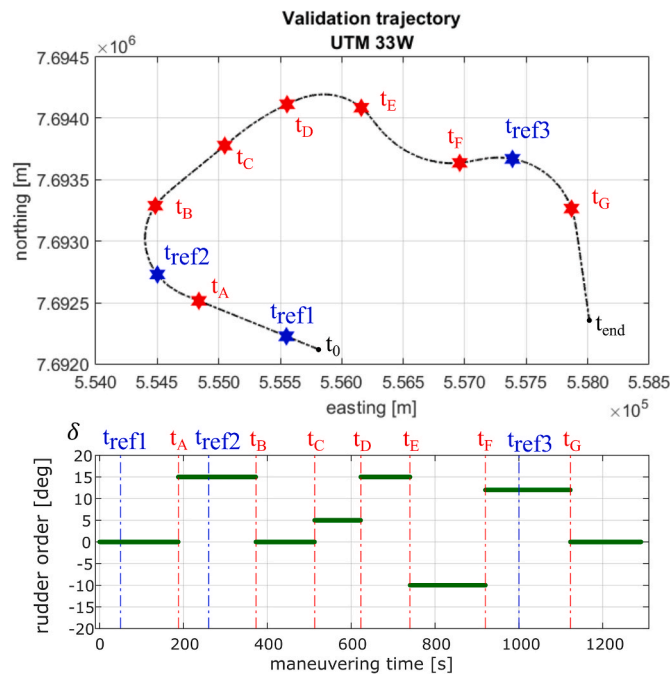


Fig. 10. Trajectory of the validation maneuver and the related rudder order. The trajectory prediction starts from these labeled time steps.

4.2. The simulated exercise for validation

To evaluate the prediction performances of both methods, a simulated maneuver performed by the same cargo carrier is executed in the simulator. Fig. 10 illustrates the trajectory alongside the corresponding rudder orders over the maneuvering time. The time steps when the predictions start are labeled in Fig. 10. The time steps highlighted in red directly follow a new rudder order, while the blue-labeled steps do not include any new rudder orders.

4.3. Parameters initialization

Two groups of parameters need to be determined in advance. The first group consists of parameters used in the ship navigation state estimation. Table 5 lists the parameters for state estimation. The values in the measurement noise covariances R are based on the sensors' performance characteristics, while the system noise covariance Q is determined through multiple trials to optimize the estimates.

The second group of parameters is related to the GRU structure and the training process (Table 6). Two hidden layers are used to correct the latent state vector h_t and the output vector y_t . To assess how well the GRU with the initialized parameters generalizes to unseen data, there are 20% of the training samples are used as the validation samples.

5. Simulation results and discussion

5.1. The training of the GRU

The training outcomes of the GRU are depicted in Fig. 11, where the training and validation loss over 100 epochs are plotted. In Fig. 11(a) and (b), the training loss curves start with higher values, gradually decreasing and stabilizing as the training proceeds. Simultaneously, the validation loss curves exhibit a similar decreasing trend, eventually converging with the training loss curves. This convergence indicates the model's proficiency in effective learning and robust generalization to new datasets. However, a distinct pattern emerges in Fig. 11(c), where the validation loss curve initially mirrors the training loss but gradually diverges after approximately 40 epochs. This deviation suggests a potential issue with overfitting, implying that the model might be excessively tailored to the training data and could encounter difficulties in generalizing to unfamiliar datasets. To mitigate this concern and obtain an optimal balance between model fit and generalization, implementing early stopping as a strategy is worth considering.

5.2. Validation of ship trajectory prediction

The ship trajectory predictions start from step t_A to t_G with new rudder orders are illustrated in Fig. 12. The ship icons shown in these plots give a direct image of the predicted position and heading in everything 15 s over the prediction horizon of 90 s. In these cases, the superiority of the GRU-PP-based prediction over the prediction horizon is evident. The prediction results can provide navigators with a comprehensive understanding of the ship's states after a decision to change the rudder order. Given the emphasis in maritime transportation on making decisions ahead of time to prevent collisions, the prediction results can offer navigators generous safety margins in both temporal and spatial domains. Additionally, early decision-making allows for a balanced consideration of safety alongside other critical factors like time and cost. Since the GRU-PP-based prediction also has the ability to assess the effectiveness of a rudder order, it can serve also as a tool in optimizing decision-making processes for collision avoidance.

The detailed quantitative analyses of the predictions start at t_A , t_C , and t_E are presented in Fig. 13 which displays the prediction errors of positions and headings. The prediction errors of positions are determined by the Euclidean distance between the actual and predicted positions. Regarding the prediction errors of headings, both the related actual and predicted headings are represented as unit vectors in a Cartesian coordinate system. Following this, the errors are calculated as the angle between these two vectors. The prediction results from the kinematic-based methods demonstrate a similar level of accuracy compared to the GRU-PP-based method during the initial stage of the prediction horizon. However, as predictions progress, the errors in the kinematic-based predictions tend to increase significantly. These significant increases in errors arise from the assumptions made about constant accelerations and yaw rates in the kinematic motion models. The increases of errors are also proportional to the magnitude of the

Table 5
The initialized parameters of ship navigation state estimation.

Model	Para.	Definition	Value	Method of estimation
CAA	dt	time interval between consecutive measurements	0.1 [s]	Estimates are acquired every 0.1 s.
	Q	noise covariance matrix of system model	$\begin{pmatrix} dt^4/20 & dt^3/8 & dt^2/6 \\ dt^3/8 & dt^2/3 & dt/2 \\ dt^2/6 & dt/2 & 1 \end{pmatrix} \bullet q_f$	A general noise covariance matrix for constant acceleration models
	R	noise covariance matrix of measurement model	$\begin{pmatrix} (0.5 \pi/180)^2 & 0 \\ 0 & (0.01 \pi/180)^2 \end{pmatrix}$	Values are referred to the sensors' performance property
CTRA	dt	time interval between consecutive measurements or updates	0.1 [s]	Estimates are acquired every 0.1 s.
	Q	noise covariance matrix of system model	$Diag(10^{-2}, 10^{-2}, 10^{-4}, 10^{-4}, 10^{-6}, 10^{-6})$	Determined by multiple trials to obtain the optimal estimates
	R	noise covariance matrix of measurement model	$Diag(1, 1, 10^{-4}, 10^{-4})$	Values are referred to the sensors' performance property
CMM	dt	time interval between consecutive measurements or updates	0.1 [s]	Estimates are acquired every 0.1 s.
	δt	time interval in the temporal discretization of nonlinear model	0.005 [s]	A trade-off value balancing accuracy and stability
	Q	noise covariance matrix of system model	$Diag(10^{-1}, 10^{-1}, 10^{-3}, 10^{-3}, 10^{-5}, 10^{-5})$	Determined by multiple trials to obtain the optimal estimates
	R	noise covariance matrix of measurement model	$Diag(1, 1, 10^{-4}, 10^{-4})$	Values are referred to the sensors' performance property
	λ	Tuning parameter used in the UKF	1.72	Recommended value suggested in (Wan and Merwe, 2000)

Table 6
The initialized parameters of the GRU.

Type	Para.	Definition	Value	Notation
Training samples	N_{train}	Total number of training samples	107	collection from 5 h' maneuvering
	N_{valid}	Total number of validation samples	22	20% of the N_{train}
Neuron network structure	n_c	Number of GRU cell	300	corresponding to input lag 300
	n_h	the number of dense layers	2	
	n_{h1}	the number of nodes in 1st dense layer	240	with activation function "ReLU"
	n_{h2}	the number of nodes in 2nd dense layer	120	with activation function "ReLU"
	n_o	the number of nodes in the output layer	900	corresponding to prediction horizon 900
Back-propagation training	lr	Fixed learning rate	0.001	
	batch	size of batch for training	64	
	epoch	epochs of training	100	proven to be converged

rudder angle. For example, predictions starting at t_C with a rudder change from 0 to 5 [deg] exhibit less errors compared to predictions starting at t_A and t_E . It is worth noting that the rise in prediction errors for heading occurs earlier than that of positions. This can imply that as for the used cargo carrier, the heading experiences a shorter response delay following a new rudder order compared to the course.

The prediction results and errors for cases without new rudder orders are depicted in Figs. 14 and 15. In these predictions, it is apparent that both prediction methods exhibit comparable performances. Particularly in the scenario beginning from t_{ref2} , the kinematic-based method surpasses the performance of the GRU-based method. It is essential to note that the training samples for the GRU always include a new rudder order in inputs. However, the presentation in Fig. 14 shows that the designed GRU can still generate reasonable predictions when inputs does not contain new rudder orders. Nonetheless, it is important to acknowledge that such predictions carry uncertainties, as evidenced by Fig. 14(b) which shows substantial prediction errors gradually.

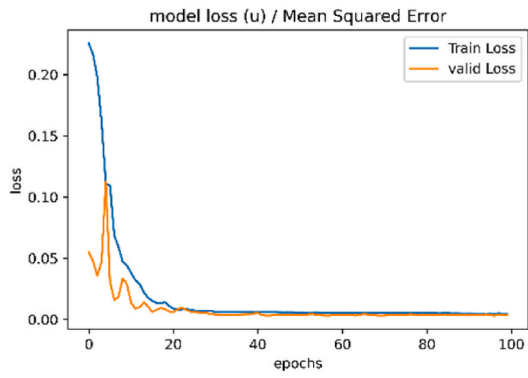
The statistical analysis of the prediction results is depicted in Figs. 16 and 17. In Fig. 16, all the prediction errors start with new rudder orders (from $t_A - t_C$) are aggregated to generate boxplots for selected time steps. It is evident that the GRU-PP-based method exhibits superior performance when predictions start with new rudder angles. Conversely, the kinematic-based prediction can only maintain better precision over a shorter duration. A similar analysis is conducted for predictions starting without rudder angle orders, i.e., the predictions from t_{ref1} , t_{ref2} , and t_{ref3} . The performance of the kinematic-based method surpasses that of the GRU-PP-based method (see Fig. 17). The kinematic-based method demonstrates its reliability during steady ship stages. Considering the strengths and weaknesses of each prediction

method, a combination of both approaches could be implemented to enhance SA in ship navigation safety and address challenges in future complex navigation environments.

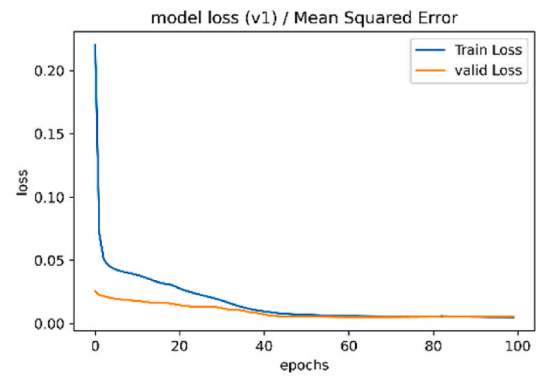
6. Conclusion

In this research, ship trajectory prediction at a local scale is examined using two distinct methods through simulated maneuvering within the UiT bridge simulator. In the kinematic-based method, trajectory predictions are achieved through combinations of kinematic motion models (CAA + CMM and CAA + CTRA). In the GRU-PP-based method, the neural network-based predictions are integrated with the pivot point and a rigid body motion-based algorithm. The GRU generates predictions for the ship's surge and sway velocities in two different reference points. These sway velocities are then utilized to determine the location of the pivot point through a predefined mapping system. Finally, trajectory prediction is achieved using the rigid body motion-based algorithm.

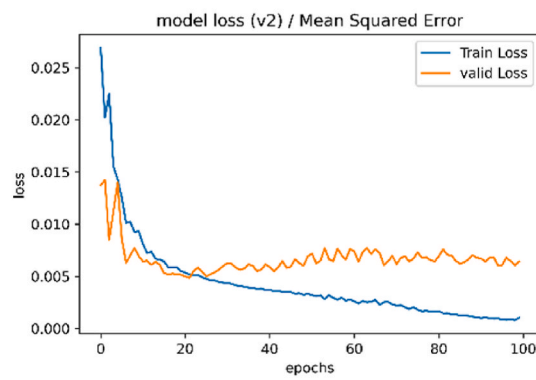
A simulated maneuver which contains multiple rudder operations is used to validate these two prediction methods. Regarding the simulation results, firstly, the kinematic-based method demonstrates superiority during the ship's steady maneuvering phases. Kinematic motion models are proven to be robust for both linear and circular steady motions of the ship. Secondly, when predictions commence with a new rudder order, the GRU-PP-based method demonstrates a significant reduction in prediction errors compared to the kinematic-based method. The significant prediction errors observed in the kinematic-based method once again highlight the limitations of kinematic motion models in the ship trajectory prediction. As the third level of Situational Awareness (SA)



(a) training loss of u

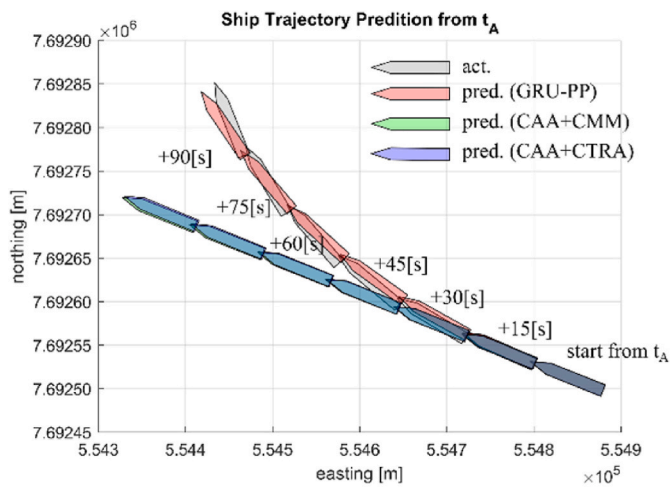


(b) training loss of v_1

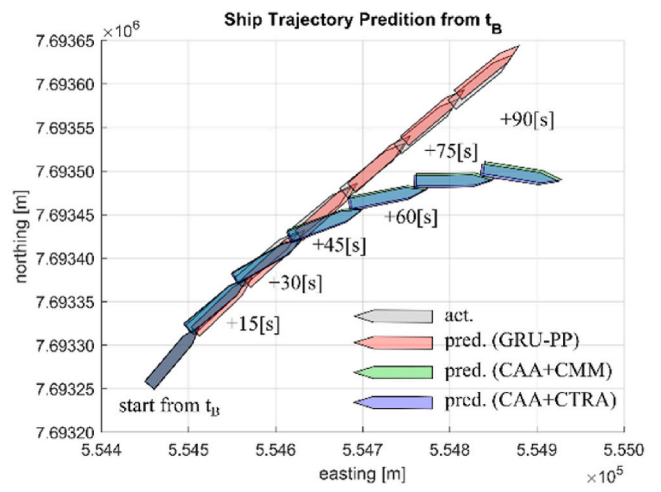


(c) training loss of v_2

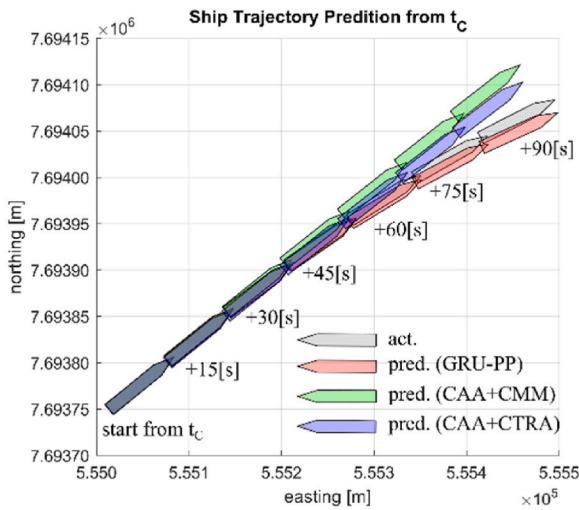
Fig. 11. Training and validation loss of the GRU.



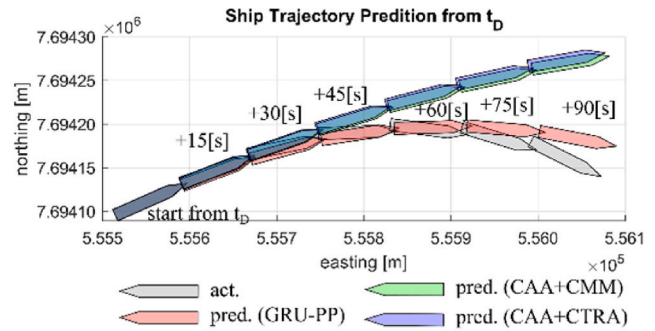
(a) Prediction from t_A



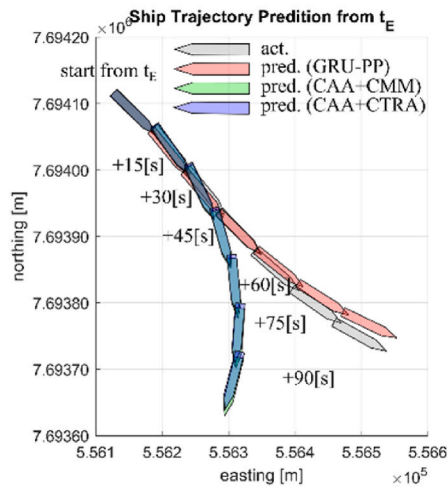
(b) Prediction from t_B



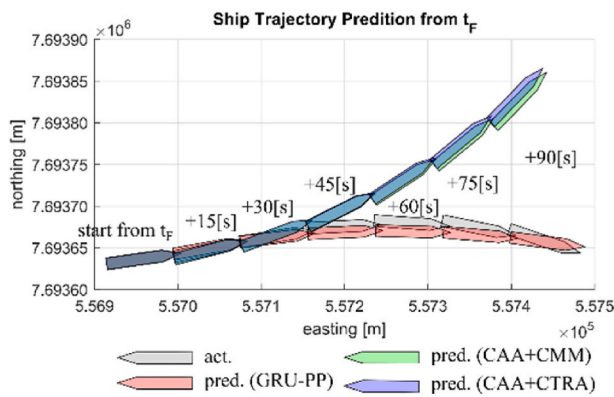
(c) Prediction from t_C



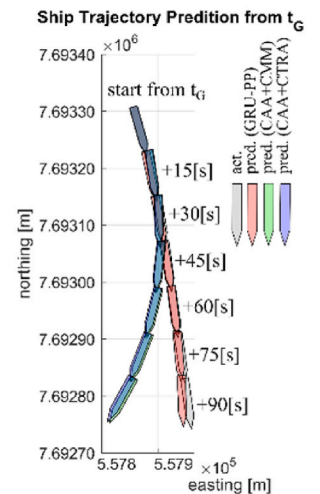
(d) Prediction from t_D



(e) Prediction from t_E

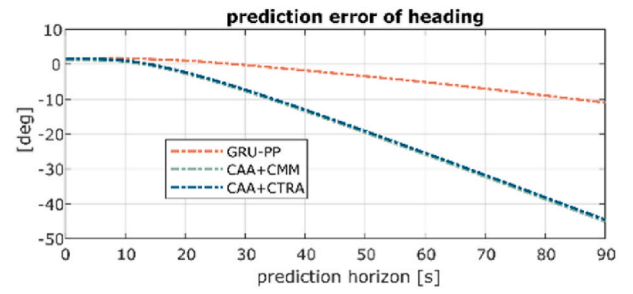
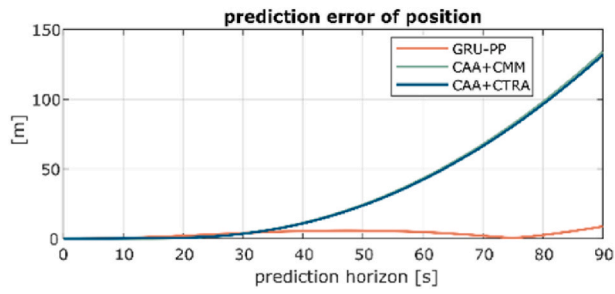


(f) Prediction from t_F



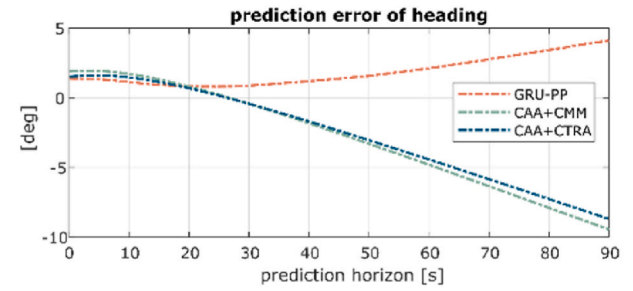
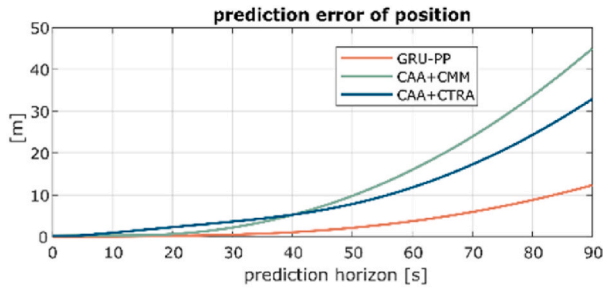
(g) Prediction from t_G

Fig. 12. Ship trajectory predictions from time steps when new rudder orders are issued.



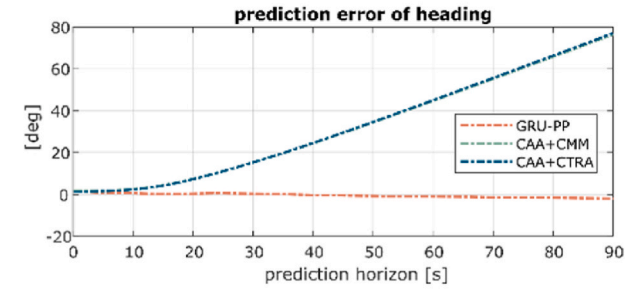
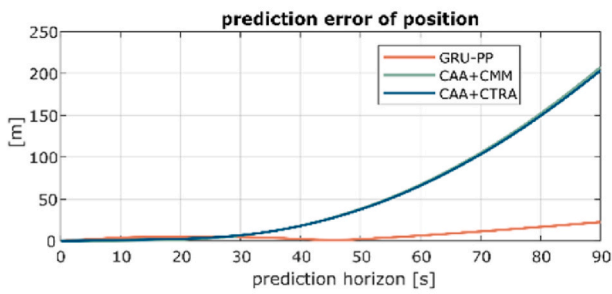
(a) error of predicted position from t_A

(b) error of predicted heading from t_A



(c) error of predicted position from t_C

(d) error of predicted heading from t_C



(e) error of predicted position from t_E

(f) error of predicted heading from t_E

Fig. 13. Prediction error from step t_A , t_C , and t_E .

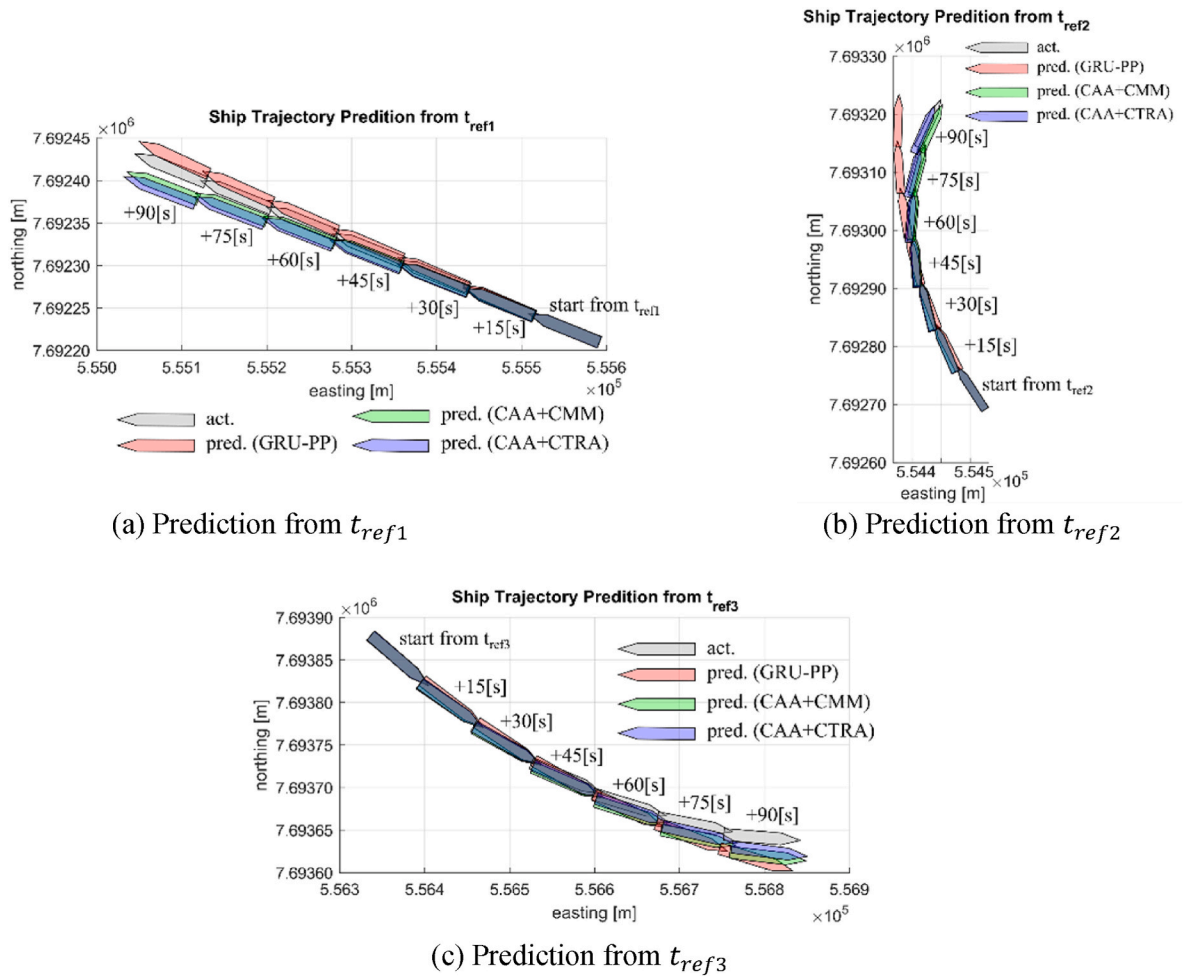
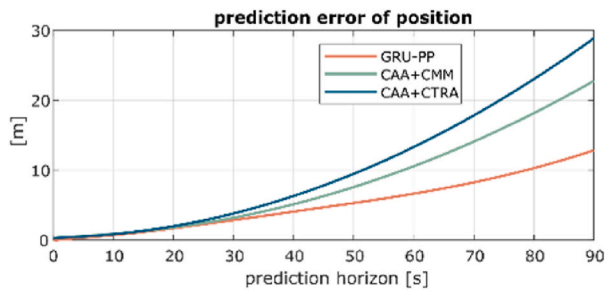
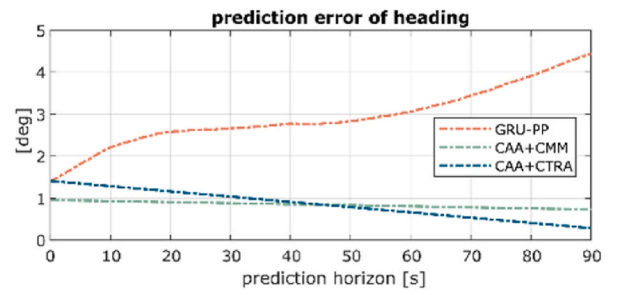


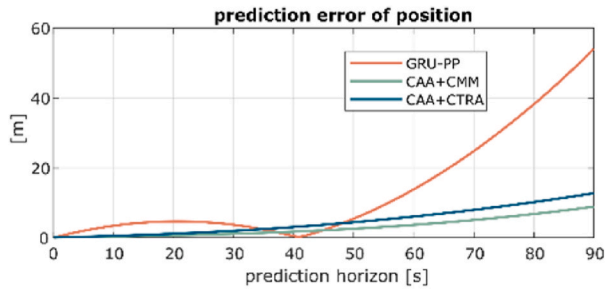
Fig. 14. Ship trajectory prediction from time steps without new rudder orders.



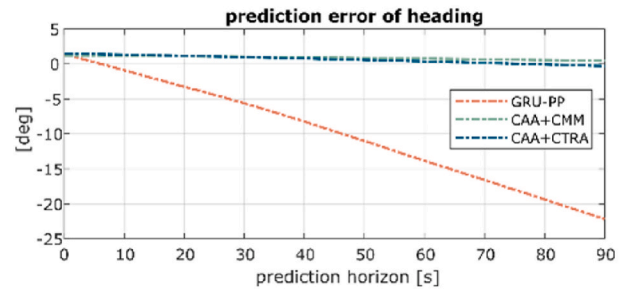
(a) error of predicted position from t_{ref1}



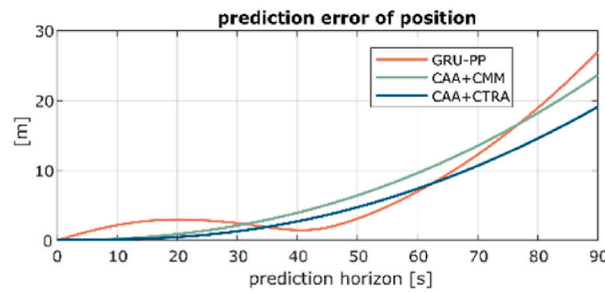
(b) error of predicted heading from t_{ref1}



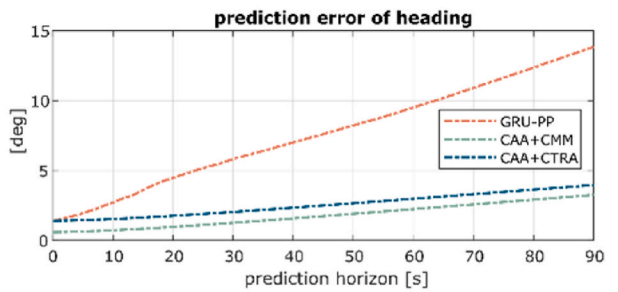
(c) error of predicted position from t_{ref2}



(d) error of predicted heading from t_{ref2}

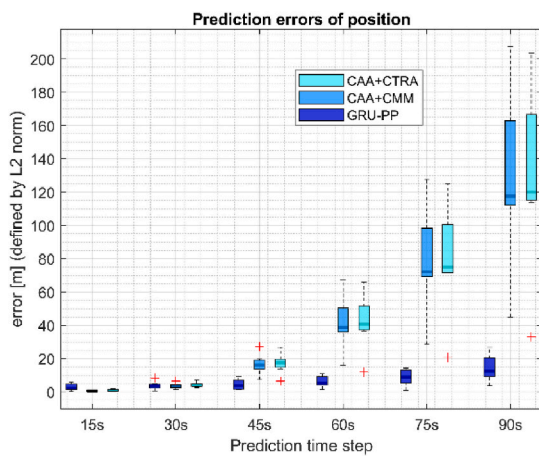


(e) error of predicted position from t_{ref3}

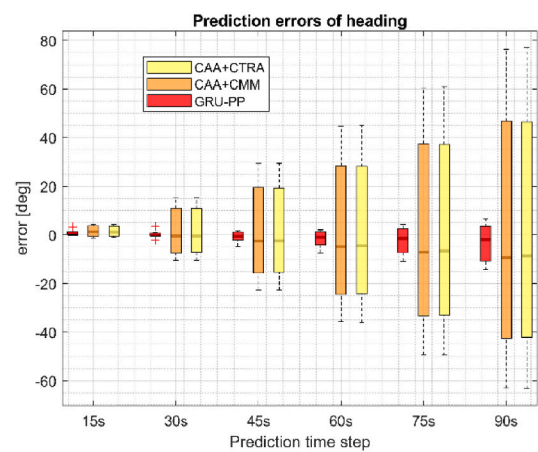


(f) error of predicted heading from t_{ref3}

Fig. 15. Prediction error from step t_{ref1} , t_{ref2} , and t_{ref3} .



(a) prediction errors of position



(b) prediction errors of heading

Fig. 16. Statistical analysis of the prediction results. Boxplots are generated using predicted values across all scenarios from time point t_A to t_G .

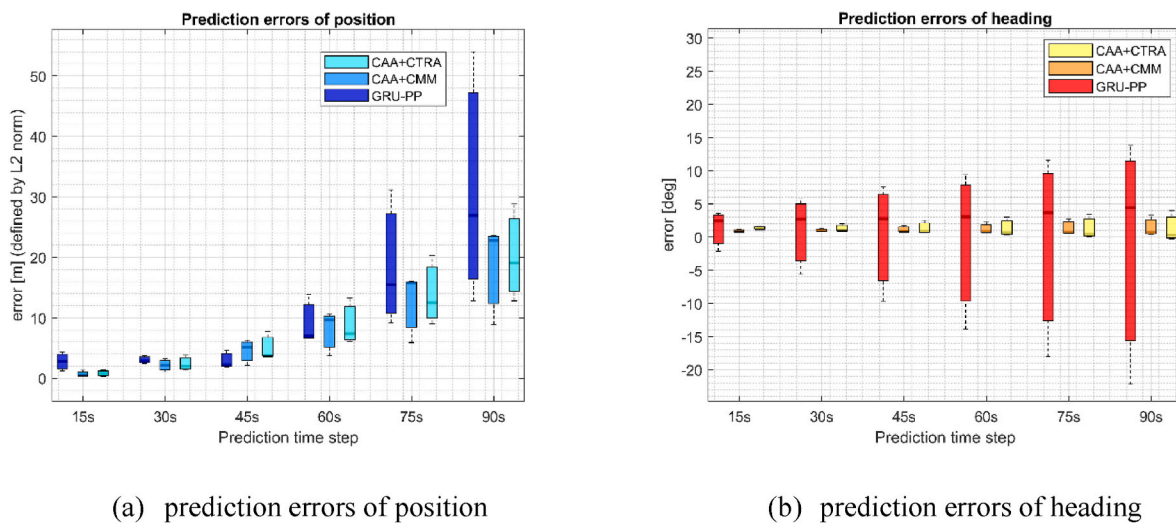


Fig. 17. Statistical analysis of the prediction results. Boxplots are generated using predicted values across all scenarios from time point t_{ref1} , t_{ref2} , and t_{ref3} .

requires projecting ship states into the near future, these predictions spanning a horizon of 90 s can thus serve as an effective tool to enhance SA.

However, the findings in this study are subject to a limitation in terms of the simulated data. The main reason is that this study focuses on demonstrating the capabilities of the proposed advanced predictors in a simulated environment. In this environment, actual ship models are highly nonlinear and remain unknown. Since the capabilities of the proposed advanced predictors are quantified, then these algorithms are ready to implement with the data sets from ocean going ships and that is the future step of this study. One should also note that real sea-trial data can encompass additional unexpected factors from the sea environment, i.e., the sensor noise may be higher due to rough wind or wave conditions, which are challenging to replicate in simulated environments. Furthermore, the training datasets used for the GRU do not incorporate features from the sea environment and weather conditions. Consequently, the GRU designed and trained using the simulated data may not be compatible with real navigation data in some situations, as the sea environment and weather conditions can significantly influence the ship's maneuvering. Therefore, future efforts will involve conducting sea-trial experiments and collecting real ship navigation data. Additional work will be required in designing the GRU to ensure that environmental factors are also reflected in the final predictions.

CRediT authorship contribution statement

Yufei Wang: Writing – original draft, Visualization, Validation, Methodology, Investigation, Formal analysis, Data curation, Conceptualization. **Lokukaluge Prasad Perera:** Writing – review & editing, Supervision, Software, Resources, Project administration, Funding acquisition. **Bjørn-Morten Batalden:** Writing – review & editing, Supervision, Resources, Project administration, Funding acquisition.

Declaration of competing interest

The authors declare that they have no known competing financial interests or personal relationships that could have appeared to influence the work reported in this paper.

Data availability

Data will be made available on request.

Acknowledgements

This work has been conducted under the Autonomous ship Program in UiT-The Arctic University of Norway, which aims to develop the digital helmsman as a part of the ship intelligence to operate future vessels supported by the MARKOM II project under the project title "Onshore Operation Center for Remotely Controlled Vessels (OOC 2023)" under the contract number PMK-2022-10014.

Appendix A. Supplementary data

Supplementary data to this article can be found online at <https://doi.org/10.1016/j.oceaneng.2024.117704>.

References

- Abilio Ramos, M., Utne, I.B., Mosleh, A., 2019. Collision avoidance on maritime autonomous surface ships: operators' tasks and human failure events. *Saf. Sci.* 116, 33–44.
- Ait Allal, A., Amrani, L., Haidine, A., Mansouri, K., Mohamed, Y., 2020. Implementation of 5G communication network for a safe operation of autonomous and conventional ships. *Int. J. Eng. Res. Afr.* 51, 229–248.
- Amro, A., Oruc, A., Gkioulos, V., Katsikas, S., 2022. Navigation data anomaly analysis and detection. *Information* 13, 104.
- Artikis, A., Zissis, D., 2021. *Guide to Maritime Informatics*. Springer Nature Switzerland AG 2021, pp. 10–11.
- AVATAR, 2023. Interreg VB North Sea Region Programme. Retrieved 8, Nov, 2023, from <https://northsearegion.eu/avатар/>.
- Bar-Shalom, Y., Li, X.R., Kirubarajan, T., 2002. State estimation for nonlinear dynamic systems. In: *Estimation with Applications to Tracking and Navigation*, pp. 371–420.
- Battle, J.A., Condomines, A.B., 2020. *Rigid Body Kinematics*. Cambridge University Press, Cambridge, England.
- Best, R.A., Norton, J.P., 1997. A new model and efficient tracker for a target with curvilinear motion. *IEEE Trans. Aero. Electron. Syst.* 33 (3), 1030–1037.
- Birkeland, Y., 2022. The First Zero Emission, Autonomous Ship: Yara International. Retrieved 8, Nov, 2023. www.yara.com/knowledge-grows/game-changer-for-the-environment/.
- Cahuantzi, R., Chen, X., Güttel, S., 2023. A comparison of LSTM and GRU networks for learning symbolic sequences. In: *Science and Information Conference*. Springer.
- Capobianco, S., Millefiori, L., Forti, N., Braca, P., Willett, P., 2020. Deep learning methods for vessel trajectory prediction based on recurrent neural networks. *IEEE Trans. Aero. Electron. Syst.* 57.
- Chang, C.-H., Kontovas, C., Yu, Q., Yang, Z., 2021. Risk assessment of the operations of maritime autonomous surface ships. *Reliab. Eng. Syst. Saf.* 207, 107324.
- Chung, J., Gulcehre, C., Cho, K., Bengio, Y., 2014. Empirical Evaluation of Gated Recurrent Neural Networks on Sequence Modeling arXiv preprint arXiv:1412.3555.
- Clark, I.C., 2005. *Ship Dynamics for Mariners*. Nautical Institute, London, England.
- Endsley, M., 1995. Endsley, M.R.: toward a theory of situation awareness in dynamic systems. *Hum. Factors: J. Human Fact. Erg. Soc.* 37, 32–64.
- Fossen, T., 2011. *Handbook of Marine Craft Hydrodynamics and Motion Control*. John Wiley & Sons, Nashville, TN.
- Fukuto, J., 2021. *Automation Levels of Automated/Autonomous Ships*. ClassNK.

- Hochreiter, S., Schmidhuber, J., 1997. Long short-term memory. *Neural Comput.* 9, 1735–1780.
- Hoem, Å., Rødseth, Ø., Fjørtoft, K., 2019. Addressing the accidental risks of maritime transportation: could autonomous shipping technology improve the statistics? *TransNav, Int. J. Marine Navig. Safety Sea Transp.* 13.
- IMO, 2019. **Autonomous Shipping**. Retrieved 8, Nov, 2023. https://en.uit.no/prosjekter/prosjektp_document_id=668855.
- Kawase, K., 2013. Concise Derivation of Extensive Coordinate Conversion Formulae in the Gauss-Krüger Projection.
- Kim, S., Yun, S., You, Y., 2021. Eco-friendly speed control algorithm development for autonomous vessel route planning. *J. Mar. Sci. Eng.* 9.
- Kim, T.-e., Perera, L., Sollid, M.-P., Batalden, B.-M., Sydnes, A., 2022. Safety challenges related to autonomous ships in mixed navigational environments. *WMU J. Maritime Aff.* 21.
- Kjerstad, N., 2021. Fremføring av skip med navigasjonskontroll [Advancement of ships with navigation and control]. *Fagbokforlaget* 11–12.
- Kohn, S., Momen, A., Wiese, E., Lee, Y.-C., Shaw, T., 2019. The consequences of purposefulness and human-likeness on trust repair attempts made by self-driving vehicles, 63, 222–226.
- Kongsberg, 2023. **Autonomous Ships Equipment/Products/Systems - Kongsberg Maritime**. Retrieved 8, Nov, 2023. <https://www.kongsberg.com/maritime/ship-types/autonomous-ships/>.
- Koo, H., Chae, J., Kim, W., 2023. Design and experiment of satellite-terrestrial integrated gateway with dynamic traffic steering capabilities for maritime communication. *Sensors* 23, 1201.
- Korotkin, A.I., 2008. *Added Masses of Ship Structures*. Springer, New York, NY.
- Lee, C.-K., Moon, S.-B., Jeong, T.-G., 2016. The investigation of ship maneuvering with hydrodynamic effects between ships in curved narrow channel. *Int. J. Nav. Archit. Ocean Eng.* 8 (1), 102–109.
- Li, M.-W., Xu, D.-Y., Geng, J., Hong, W.-C., 2022. A hybrid approach for forecasting ship motion using CNN-GRU-AM and GCWOA. *Appl. Soft Comput.* 114.
- Lipton, Z.C., Berkowitz, J., Elkan, C., 2015. A Critical Review of Recurrent Neural Networks for Sequence Learning arXiv preprint arXiv:1506.00019.
- Lu, Z., Kang, L., Gao, S., Meng, Q., 2018. Determination of minimum distance to obstacle avoidance in the Singapore strait. *Transport. Res. Rec.: J. Transport. Res. Board* 2672.
- MEGURI2040, 2022. **The Nippon Foundation MEGURI2040 Fully Autonomous Ship Program**. Retrieved 8, Nov, 2023, from. <https://www.nippon-foundation.or.jp/en/what/projects/meguri2040>.
- Munim, Z., 2019. Autonomous ships: a review, innovative applications and future maritime business models. *Supply Chain Forum* 20, 266–279.
- Murray, B., Perera, L.P., 2021. An AIS-based deep learning framework for regional ship behavior prediction. *Reliab. Eng. Syst. Saf.* 215, 107819.
- NFAS, 2017. Definition for Autonomous Merchant Ships, Norwegian Forum for Autonomous Ships.
- Oruc, A., Amro, A., Gkioulos, V., 2022. Assessing cyber risks of an INS using the MITRE ATT&CK framework. *Sensors* 22, 8745.
- Pascanu, R., Mikolov, T., Bengio, Y., 2013. On the difficulty of training recurrent neural networks. In: *International Conference on Machine Learning*. Pmlr.
- Perera, L., 2019. Deep learning towards autonomous ship navigation and possible COLREGS failures. *J. Offshore Mech. Arctic Eng.*
- Perera, L., Batalden, B.-M., 2019. Possible COLREGS Failures under Digital Helmsman of Autonomous Ships.
- Perera, L., Guedes Soares, C., 2012. Detections of Potential Collision Situations by Relative Motions of Vessels under Parameter Uncertainties, pp. 705–713.
- Perera, L., Murray, B., 2019. Situation awareness of autonomous ship navigation in a mixed environment under advanced ship predictor. In: *Proceedings of the 38th International Conference on Ocean, Offshore and Arctic Engineering (OMAE 2019)*. Glasgow, Scotland, UK.
- Perera, L., Oliveira, P., Guedes Soares, C., 2012. Maritime traffic monitoring based on vessel detection, tracking, state estimation, and trajectory prediction. *IEEE Trans. Intell. Transport. Syst.* 13.
- Perera, L.P., 2017. Navigation vector based ship maneuvering prediction. *Ocean Eng.* 138, 151–160.
- Porathe, T., Prison, J., Man, Y., 2014. Situation awareness in remote control centres for unmanned ships. In: *Proceedings of Human Factors in Ship Design & Operation*, London, UK.
- Rødseth, Ø., 2019. Defining ship autonomy by characteristic factors. In: *Proceedings of ICMAS 2018 Busan, Korea*. SINTEF Academic Press.
- Rødseth, Ø.J., Wennersberg, L.A.L., Nordahl, H., 2023. Improving safety of interactions between conventional and autonomous ships. *Ocean Eng.* 284.
- Seo, S.-G., 2016. Safer and more efficient ship handling with the pivot point concept. *TransNav, Int. J. Marine Navig. Safety Sea Transp.* 10, 605–612.
- Suo, Y., Chen, W., Claramunt, C., Yang, S., 2020. A ship trajectory prediction framework based on a recurrent neural network. *Sensors* 20.
- Syed, M.A., Ahmed, I., 2023. A CNN-LSTM architecture for marine vessel track association using automatic identification system (AIS) data. *Sensors* 23. <https://doi.org/10.3390/s23146400>.
- Thombre, S., Zhao, Z., Ramm-Schmidt, H., García, J.M.V., Malkamäki, T., Nikolskiy, S., Hammarberg, T., Nuortie, H., Bhuiyan, M.Z.H., Särkkä, S., Lehtola, V.V., 2022. Sensors and ai techniques for situational awareness in autonomous ships: a review. *IEEE Trans. Intell. Transport. Syst.* 23 (1), 64–83.
- Tzeng, C.-Y., 1998. Analysis of the pivot point for a turning ship. *J. Mar. Sci. Technol.* 6 (1).
- UiT, 2021. **UiT Autonomous Ship Program**. Retrieved 8, Nov, 2023, from. https://en.uit.no/prosjekter/prosjekt?p_document_id=668855.
- Veitch, E., Andreas Alsos, O., 2022. A systematic review of human-AI interaction in autonomous ship systems. *Saf. Sci.* 152, 105778.
- Wan, E.A., Merwe, R.V.D., 2000. The unscented Kalman filter for nonlinear estimation. In: *Proceedings of the IEEE 2000 Adaptive Systems for Signal Processing, Communications, and Control Symposium (Cat. No.00EX373)*.
- Wang, C., Ren, H., Li, H., 2020. Vessel trajectory prediction based on AIS data and bidirectional GRU. In: *2020 International Conference on Computer Vision, Image and Deep Learning (CVIDL)*.
- Wang, Y., Perera, L.P., Batalden, B.-M., 2023a. Coordinate conversion and switching correction to reduce vessel heading-related errors in high-latitude navigation. In: *The 22nd World Congress of the International Federation of Automatic Control (IFAC 2023)*. Yokohama, Japan, pp. 11590–11595. 56-2.
- Wang, Y., Perera, L.P., Batalden, B.-M., 2023b. Kinematic motion models based vessel state estimation to support advanced ship predictors. *Ocean Eng.* 286, 115503.
- Wickens, C., Williams, A., Clegg, B., Smith, C.A.P., 2019. Nautical collision avoidance: the cognitive challenges of balancing safety, efficiency, and procedures. *Hum. Factors: J. Human Fact. Erg. Soc.* 62.
- Wolsing, K., Roepert, L., Bauer, J., Wehrle, K., 2022. Anomaly detection in maritime AIS tracks: a review of recent approaches. *J. Mar. Sci. Eng.* 10 <https://doi.org/10.3390/jmse10010112>.
- Wróbel, K., Montewka, J., Kujala, P., 2017. Towards the assessment of potential impact of unmanned vessels on maritime transportation safety. *Reliab. Eng. Syst. Saf.* 165, 155–169.
- Yang, S., Yu, X., Zhou, Y., 2020. LSTM and GRU neural network performance comparison study: taking yelp review dataset as an example. In: *2020 International Workshop on Electronic Communication and Artificial Intelligence (IWECAL)*.
- Zhang, S., Wang, L., Zhu, M., Chen, S., Zhang, H., Zeng, Z., 2021. A Bi-directional LSTM ship trajectory prediction method based on attention mechanism. In: *2021 IEEE 5th Advanced Information Technology, Electronic and Automation Control Conference (IAEAC)*.
- Zhao, L., Shi, G., Yang, J., 2018. Ship trajectories pre-processing based on AIS data. *J. Navig.* 71 (5), 1210–1230.
- Zhou, X., Liu, Z., Wu, Z., Wang, F., 2019. Quantitative processing of situation awareness for autonomous ships navigation. *TransNav, Int. J. Marine Navig. Safety Sea Transp.* 13, 25–31.